The Fate of Carbon during Earth's Core–Mantle Differentiation

I. Blanchard[1]*, E. S. Jennings[2], I. A. Franchi[3], X. Zhao[3], S. Petitgirard[1], N. Miyajima[1], S. A. Jacobson[4], D.C. Rubie[1]

[1] Bayerisches Geoinstitut, Universität Bayreuth, 95440 Bayreuth, Germany

[2] Department of Earth and Planetary Sciences, Birkbeck, University of London, Malet Street, London WC1E 7HX, UK

[3] School of Physical Sciences, Open University, Milton Keynes MK7 6AA, UK

[4] Department of Earth and Environmental Sciences, Michigan State University, East Lansing, MI 48824, USA

*Corresponding author: ingrid.blanchard@uni-bayreuth.de

This manuscript is a non-peer reviewed pre-print submitted to EarthArXiv.

The preprint was submitted to Nature for peer review.

Abstract

Carbon is an essential element for the existence and evolution of life on Earth, constitutes up to 50% of dry biomass, and is likely a requirement for all life in the universe. Its high abundance in Earth's crust and mantle (the Bulk Silicate Earth, BSE) is surprising because carbon is strongly siderophile (metal-loving) and should have segregated almost completely into Earth's core during accretion[1–3]. Estimates of the concentration of carbon in the mantle lie mostly in the range of 80–120 ppm[4,5], which is much higher than expected based on simple models of core–mantle differentiation[2,6,7]. Here we show through experiments at 49–71 GPa and 3600–4000 K that carbon is significantly less siderophile at such conditions than at the low pressures (≤ 3 GPa) of previous studies[1–3,8]. We derive a new parameterization of the pressure–temperature dependence of the metal–silicate partitioning of carbon and apply this in a state-of-the-art model of planet formation and differentiation[9,10] that is based on astrophysical N-body accretion simulations. Results show that BSE carbon concentrations increase strongly starting at a very early stage of Earth's accretion and, depending on the concentration of carbon in accreting bodies, can easily reach or exceed estimated BSE values. In contrast, simple models of "continuous core formation"[11–13] require all BSE carbon to be accreted after core formation ended, but this is not consistent with astrophysical models of accretion.

The   extents to which the volatile contents of terrestrial planets were determined by the processes of accretion and core formation, impact-driven volatile loss, and addition of a late veneer subsequent to core formation are highly controversial[9,14–17]. The Earth is considered to have formed from bodies of chondritic composition, although it is unlikely that any particular chondrite group constituted the sole building blocks of the planet[18]. Different classes of chondrites have varying carbon concentrations, but importantly, such concentrations are all

2

high, at the weight percent level[19]. This is far in excess of the concentration of carbon present in the Bulk Silicate Earth (BSE) today, which is currently estimated to be 80–120 ppm[4,5] or possibly as high as 765 ± 300 ppm[20]. Additionally, the metal–silicate partition coefficient of carbon at low pressures and temperatures (≤ 13 GPa and ≤ 2000 K) is very high ($D > 1000$; see D defined in Eq. 2 and ref.[1–3,21]). Consequently, almost all carbon should have partitioned into the core during its formation, leaving the mantle almost completely depleted in this element. Several explanations have been proposed for the BSE C concentration, including crystallization of C-rich phases (e.g. diamond) from a C-saturated magma ocean, imperfect metal–silicate equilibration during core formation, accretion of a "late veneer" after the end of core formation, and carbon outgassing from the core[1,3,22].

Here we present the results of experiments that determine the metal–silicate partition coefficient of carbon at conditions that are likely similar to that of metal–silicate equilibration/segregation during core formation[23], and that are at much higher pressures and temperatures than those of previous studies. We use the results in a state-of-the art model that combines accretion and core–mantle differentiation[9,10], and so we show that the present BSE carbon concentration is the direct consequence of core formation.

We performed laser-heated diamond anvil cell (LH-DAC) experiments to reproduce the pressures and temperatures of the putative conditions of Earth's core-mantle differentiation in the laboratory. We performed experiments at 49–71 GPa and 3600–4000 K for a few tens of seconds using a double-sided laser-heated system (see Methods section for details). After melting and quenching at high pressure, our recovered samples consisted of a central metallic sphere surrounded by quenched silicate glass, as observed in previous similar studies[24–26] (Fig. 1a). Samples were prepared for analysis using a Focused Ion Beam system and analysed for major elements using Electron Probe Microanalysis (EPMA see Methods section). To measure the concentrations of carbon in the quenched silicate melt, we used NanoSIMS, for which we

synthesized appropriate standards (the carbon contents of which were analysed by FTIR; see the Methods section).

We calculated the oxygen fugacities of our experiments relative to the iron-wüstite redox buffer (ΔIW), based on the assumption of ideal mixing of both phases (as justified by the high temperatures):

$$\Delta IW = 2\log\frac{X_{FeO}}{X_{Fe}}.$$ (1)

Oxygen fugacities of our experiments lie between -0.9 and -1.5 log units relative to the IW buffer (Table 1). The concentration of carbon in the metal lies in the range from 5 to 9.4 wt.% and in the quenched silicate melt varies from 545 to 2800 ppm. The concentrations of carbon in the quenched silicate melt are much higher than concentrations observed in low P–T experiments which are typically 10–200 ppm[1–3,8]. Thus, metal–silicate partition coefficients for carbon are 24–166 (Table 1) and are 1–2 orders of magnitude lower than those determined in previous low-pressure studies.

In order to understand the metallic phase better, we obtained images with SEM and TEM of the sample BAS C 39 (Fig. 1), and we performed electron diffraction analyses that show the presence of stoichiometric Fe_7C_3 inclusions in the quenched metal (Fig. 1b). To further investigate the quench textures (Fig. 1c), we performed scanning TEM-energy dispersive spectroscopy (EDS) mapping to identify Si-O-rich exsolved inclusions in the metal phase (Fig. 1d) along with a C-rich domain that could be an exsolved diamond, as also observed in previous similar experiments[27].

To understand the effects of pressure and temperature on the metal–silicate partitioning of carbon, we assembled a dataset for our model from previous studies to supplement our new results (Fig. 2). However, only some published experiments are relevant to core formation because prior studies were often focussed on the effects of silicate melt composition[2], fO_2 [28,29], and the interaction of carbon with elements in the metal[7]. The partitioning of carbon is affected

by the ratio of non-bridging oxygens to tetrahedral cations[2] (NBO/T), so we only included data

from the literature for which NBO/T lies in a narrow range (0.5–1.5); the range for our samples

is 0.56–1.34. We also only included data from previous low P–T studies with low

concentrations (< 1 wt.%) of light elements (S, N, O, Si) in the metal because the interaction

between carbon and other light elements may be significant[6] but is poorly constrained. As a

consequence, we also excluded very low fO_2 data ($\Delta IW < -3$), as they are often associated with

high concentrations of Si in the metal. On the other hand, our high P-T samples contain

significant concentrations of oxygen and silicon in the metallic phase, as is typical for high

temperature experiments[24,25]. By combining these two datasets, we thereby empirically include

the interaction effects of these light elements in the regression presented below, because the

concentrations of O and Si in metal are generally low during core formation at low P–T

conditions[11,31] consistent with the data[1-3,8] selected from previous studies, whereas at high P–T

conditions such concentrations become high[30,31], which is consistent with the present study.

Interactions of carbon with oxygen and silicon in the metal of our experiments might be at least

partly responsible for the scatter of our data (Fig. 2). Finally, we did not use literature data for

which the silicate phase did not quench to a glass, because the quality of SIMS analyses may

be compromised[1]. In Fig. 2, we present a comparison of our data together with the selected data

from the literature as a function of temperature and pressure.

The metal–silicate partition coefficient of carbon (D_C) is calculated as:

$$D_C = \frac{X_C^{metal}}{X_{(CO3)2-}^{silicate}}, \qquad (2)$$

where X is the mole fraction of the element in the phase of interest. D is a function of several

parameters, including pressure (P), temperature (T), and oxygen fugacity.

To remove the effect of oxygen fugacity on D values, we use the distribution coefficient K_D:

$$K_D = \frac{D_C}{(D_{Fe})^{n/2}}, \qquad (3)$$

where n is the valence of C when dissolved in silicate liquid, which is 4 for carbon in this case[32]. Based on the aforementioned data selection, we fitted previously– published data[1–3,8] along with our new results to derive the following expression:

$$\log K_{\mathrm{D}} = -1(\pm 0.5) + \frac{4842(\pm 920)}{T} + 31(\pm 19)\frac{P}{T}. \qquad (4)$$

This relation shows that carbon becomes less siderophile with increasing depth along a magma ocean geotherm, and predicts K_{D} values fairly well for both low and high P–T experiments (see Extended Data Fig. S3).

We used the parameterization of Eq. 4 in a combined model of accretion and core–mantle differentiation[10]. This model is based on N-body accretion simulations that typically start with 80–220 Mars-size embryos (initially located between 0.7 and 3.0 AU) that are embedded in a protoplanetary disk consisting of a few thousand much smaller planetesimals that are initially distributed over a heliocentric distance of 0.7 to ~ 9.5 AU. In the accretion simulations, planets typically grow from the starting embryos through accretional collisions with other embryos and planetesimals. Each collision potentially involves a core formation event during which accreted metal equilibrates with silicate liquid in a magma ocean and then segregates to the proto-core. By modelling metal–silicate equilibration using a mass balance approach, the evolving compositions of the mantles and cores of all accreting bodies are tracked. The approach requires that the compositions of all starting bodies are defined, with refractory element compositions matching CI chondrites. An oxidation gradient in the protoplanetary disk defines the oxygen content of starting bodies, which is the main compositional variable. Embryos and planetesimals that formed within ~1 AU of the Sun are highly reduced but with increasing heliocentric distance are increasingly oxidized[9,33]. Planetesimals originating from beyond ~ 4.5 AU are fully oxidized, contain no metal, and have an H_2O content of ~ 20 wt.%. An important

feature of the model is that accreted metal only equilibrates with a small fraction of the silicate mantle – which is quantified using a hydrodynamic model of the interaction of metal and silicate as material from the impactor's core sinks in a magma ocean[34].

Here we use the "Grand Tack"[35,36] accretion simulation "4:1-0.5-8"[9] with the same model parameters as in our previous study[10]. We first assume that carbon is accreted to Earth only in bodies that originate beyond 4.5 AU and that their average C concentration is 1.6 wt.% (an approximately mean carbonaceous chondrite (CI, CM, CO and CV) value). The mantle C abundance increases throughout accretion from a very early stage and finally reaches the BSE value of 80–120 ppm (Fig. 3). However, in this model the final concentration of C in the core is 47 ppm which means that the carbon concentration of the bulk Earth is only 83 ppm, i.e. far below the lowest estimate of 520 ppm[20]. We have therefore developed a scenario that results in a bulk concentration of ~520 ppm. We assume that bodies from beyond 4.5 AU contain on average 1.6 wt.% carbon and that C concentrations in bodies originating at < 4.5 AU decrease along a linear gradient to reach a value of zero at a heliocentric distance of 1.88 AU. This is based on the condensation of volatile elements such C increasing with heliocentric distance as temperatures decrease and is analogous to a concentration gradient derived for sulfur[10]. The model then predicts a final mantle C concentration of 314 ppm (Fig. 3), a core concentration of 950 ppm and a bulk Earth concentration of 518 ppm. This calculation is not unique because the concentration (1.6 wt.% C) and distance (1.88 AU) parameters are of course correlated. Furthermore, if water-rich outer solar system planetesimals have concentrations of C exceeding 1.6 wt.%, then it is possible to obtain mantle concentrations consistent with the estimate of 765 ± 300 ppm[20] because C delivered to Earth's mantle is inefficiently extracted by subsequent core formation similar to S and the HSEs[10], as explained below. In summary, the final mantle abundance of Earth exceeds 200 ppm for all plausible C concentrations of the initial bodies in the protoplanetary disk.

A BSE carbon concentration of > 200 ppm is considerably higher than the estimate of 100 ± 20 ppm[4,5]. If the 100 ± 20 ppm value is correct, an additional process, that is not included in our model, may have transported excess carbon to the core. There is experimental evidence that the pressure-induced disproportionation of $Fe^{2+} \rightarrow Fe^{3+} + Fe$ in deep magma oceans causes the formation of dispersed Fe metal droplets[37,38]. The gravitational segregation of these metal droplets could have transported the excess carbon to the core, leaving ~100 ppm in the mantle and resulting in 0.14 wt.% C in the core.

There are two critical features of the accretion/differentiation model that explain why the BSE carbon concentration is not efficiently extracted during core formation in spite of its siderophile behaviour. First, bodies originating from the outer solar system are water ice-bearing and so fully oxidize and contain no metal. Thus, there is no core formation event when they are accreted and the delivered C remains in the magma ocean/mantle. Second, when differentiated metal-bearing bodies are accreted, the metal of the impactor only equilibrates with a fraction of the target's mantle, of which the value depends on the size of the impactor's core and the depth of the magma ocean[9,34]. The fractions of the mantle that equilibrate with metal in the present simulation are 0.16 to 2.5% for planetesimal impacts and 2.6 to 9.9% for embryo impacts. Consequently, core formation events are extremely inefficient at removing carbon from the bulk of the mantle and transferring it to the core. These two critical features are absent in the models of "continuous core formation" that are currently applied in many studies of Earth's differentiation[12,13]; the result of a continuous core formation model for carbon is presented in the supplementary information for comparison. In such models all accreted material is assumed to contain metal and it is assumed (unrealistically) that all accreted metal equilibrates chemically with the entire Earth's mantle. Consequently, such models predict that essentially the entire BSE carbon budget has to be delivered during late accretion, i.e. after core formation has ended (see supplementary Information and Extended Data Fig. S3). We know of no

astrophysical accretion simulations that would support this scenario which requires the accretion of carbon-poor material during core formation and carbon-rich material afterwards during late accretion.

Bibliography

1. Dasgupta, R., Chi, H., Shimizu, N., Buono, A. S. & Walker, D. Carbon solution and partitioning between metallic and silicate melts in a shallow magma ocean: implications for the origin and distribution of terrestrial carbon. *Geochim. Cosmochim. Acta* **102**, 191–212 (2013).

2. Chi, H., Dasgupta, R., Duncan, M. S. & Shimizu, N. Partitioning of carbon between Fe-rich alloy melt and silicate melt in a magma ocean - Implications for the abundance and origin of volatiles in Earth, Mars, and the Moon. *Geochim. Cosmochim. Acta* (2014). doi:10.1016/j.gca.2014.04.046

3. Armstrong, L. S., Hirschmann, M. M., Stanley, B. D., Falksen, E. G. & Jacobsen, S. D. Speciation and solubility of reduced C-O-H-N volatiles in mafic melt: Implications for volcanism, atmospheric evolution, and deep volatile cycles in the terrestrial planets. *Geochim. Cosmochim. Acta* (2015). doi:10.1016/j.gca.2015.07.007

4. Dasgupta, R. & Hirschmann, M. M. The deep carbon cycle and melting in Earth's interior. *Earth Planet. Sci. Lett.* **298**, 1–13 (2010).

5. Hirschmann, M. M. Constraints on the early delivery and fractionation of Earth's major volatiles from C/H, C/N, and C/S ratios. *Am. Mineral.* (2016). doi:10.2138/am-2016-5452

6. Li, Y., Dasgupta, R. & Tsuno, K. The effects of sulfur, silicon, water, and oxygen fugacity on carbon solubility and partitioning in Fe-rich alloy and silicate melt systems at 3 GPa and 1600^ C: Implications for core–mantle differentiation and degassing of magma oceans and reduced planet. *Earth Planet. Sci. Lett.* **415**, 54–66 (2015).

7. Li, Y., Dasgupta, R., Tsuno, K., Monteleone, B. & Shimizu, N. Carbon and sulfur budget of the silicate Earth explained by accretion of differentiated planetary embryos. *Nat. Geosci.* (2016). doi:10.1038/ngeo2801

8. Stanley, B. D., Hirschmann, M. M. & Withers, A. C. Solubility of COH volatiles in graphite-saturated martian basalts. *Geochim. Cosmochim. Acta* (2014). doi:10.1016/j.gca.2013.12.013

9.   Rubie, D. C. *et al.* Accretion and differentiation of the terrestrial planets with implications for the compositions of early-formed Solar System bodies and accretion of water. *Icarus* **248**, 89–108 (2015).

10.   Rubie, D. C. *et al.* Highly siderophile elements were stripped from Earth's mantle by iron sulfide segregation. *Science (80-.).* **353**, 1141–1144 (2016).

11.   Wade, J. & Wood, B. J. Core formation and the oxidation state of the Earth. *Earth Planet. Sci. Lett.* **236**, 78–95 (2005).

12.   Wood, B. J., Walter, M. J. & Wade, J. Accretion of the Earth and segregation of its core. *Nature* **441**, 825–833 (2006).

13.   Righter, K. *et al.* Effect of silicon on activity coefficients of siderophile elements (Au, Pd, Pt, P, Ga, Cu, Zn, and Pb) in liquid Fe: Roles of core formation, late sulfide matte, and late veneer in shaping terrestrial mantle geochemistry. *Geochim. Cosmochim. Acta* **232**, 101–123 (2018).

14.   Albarède, F. Volatile accretion history of the terrestrial planets and dynamic implications. *Nature* **461**, 1227–1233 (2009).

15.   Wood, B. J., Halliday, A. N. & Rehkämper, M. Volatile accretion history of the Earth. *Nature* **467**, E6–E7 (2010).

16.   Norris, C. A. & Wood, B. J. Earth's volatile contents established by melting and vaporization. *Nature* **549**, 507–510 (2017).

17.   Siebert, J. *et al.* Chondritic Mn/Na ratio and limited post-nebular volatile loss of the Earth. *Earth Planet. Sci. Lett.* **485**, 130–139 (2018).

18.   Drake, M. J. & Righter, K. Determining the composition of the Earth. *Nature* **416**, 39–44 (2002).

19.   Wasson, J. T. & Kallemeyn, G. W. Compositions of chondrites. *Philos. Trans. R. Soc. London A Math. Phys. Eng. Sci.* **325**, 535–544 (1988).

20.   Marty, B. The origins and concentrations of water, carbon, nitrogen and noble gases on Earth. *Earth Planet. Sci. Lett.* (2012). doi:10.1016/j.epsl.2011.10.040

21.   Tsuno, K., Grewal, D. S. & Dasgupta, R. Core-mantle fractionation of carbon in Earth and Mars: The effects of sulfur. *Geochim. Cosmochim. Acta* (2018). doi:10.1016/j.gca.2018.07.010

22.   Dasgupta, R. Ingassing, Storage, and Outgassing of Terrestrial Carbon through Geologic Time. *Rev. Mineral. Geochemistry* (2013). doi:10.2138/rmg.2013.75.7

23.   Li, J. & Agee, C. B. Geochemistry of mantle-core differentiation at high pressure. *Nature* **381**, 686–689 (1996).

24.   Siebert, J., Badro, J., Antonangeli, D. & Ryerson, F. J. Metal-silicate partitioning of Ni and Co in a deep magma ocean. *Earth Planet. Sci. Lett.* **321**–**322**, 189–197 (2012).

25.   Blanchard, I., Siebert, J., Borensztajn, S. & Badro, J. The solubility of heat-producing elements in Earth's core. *Geochemical Perspect. Lett.* 1–5 (2017). doi:10.7185/geochemlet.1737

26.   Suer, T. A., Siebert, J., Remusat, L., Menguy, N. & Fiquet, G. A sulfur-poor terrestrial core inferred from metal–silicate partitioning experiments. *Earth Planet. Sci. Lett.* **469**, 84–97 (2017).

27.   Lord, O. T., Walter, M. J., Dasgupta, R., Walker, D. & Clark, S. M. Melting in the Fe-C system to 70 GPa. *Earth Planet. Sci. Lett.* **284**, 157–167 (2009).

28.   Li, Y., Dasgupta, R. & Tsuno, K. Carbon contents in reduced basalts at graphite saturation: Implications for the degassing of Mars, Mercury, and the Moon. *J. Geophys. Res. Planets* (2017). doi:10.1002/2017JE005289

29.   Malavergne, V. *et al.* Experimental constraints on the fate of H and C during planetary core-mantle differentiation. Implications for the Earth. *Icarus* **321**, 473–485 (2019).

30.   Mann, U., Frost, D. J. & Rubie, D. C. Evidence for high-pressure core-mantle differentiation from the metal-silicate partitioning of lithophile and weakly-siderophile elements. *Geochim. Cosmochim. Acta* **73**, 7360–7386 (2009).

31.   Frost, D. J. *et al.* Partitioning of oxygen between the Earth's mantle and core. *J. Geophys. Res.* **115**, (2010).

32.   Shcheka, S. S., Wiedenbeck, M., Frost, D. J. & Keppler, H. Carbon solubility in mantle minerals. *Earth Planet. Sci. Lett.* **245**, 730–742 (2006).

33.   Monteux, J., Golabek, G. J., Rubie, D. C., Tobie, G. & Young, E. D. Water and the Interior Structure of Terrestrial Planets and Icy Bodies. *Space Sci. Rev.* **214**, (2018).

34.   Deguen, R., Olson, P. & Cardin, P. Experiments on turbulent metal-silicate mixing in a magma ocean. *Earth Planet. Sci. Lett.* **310**, (2011).

35.   O'Brien, D. P., Walsh, K. J., Morbidelli, A., Raymond, S. N. & Mandell, A. M. Water Delivery and Giant Impacts in the ' Grand Tack ' Scenario. *Icarus* (2014). doi:10.1016/j.icarus.2014.05.009

36.   Walsh, K. J., Morbidelli, A., Raymond, S. N., O'Brien, D. P. & Mandell, A. M. A low mass for Mars from Jupiter's early gas-driven migration. *Nature* **475**, 206–209 (2011).

37.   Armstrong, K., Frost, D. J., McCammon, C. A., Rubie, D. C. & Boffa Ballaran, T. Deep magma ocean formation set the oxidation state of Earth's mantle. *Science (80-.).* **365**, 903–906 (2019).

38. Frost, D. J. *et al.* Experimental evidence for the existence of iron-rich metal in the Earth's lower mantle. *Nature* **428**, 409–412 (2004).

Table

*Table 1: **Experimental conditions of carbon partitioning experiments.***

Run #	BAS C 50	BAS C 60	BAS C 39	BAS C 42
P (GPa)	60	71	49	56
T (K)	3800	4000	3600	3700
ΔIW	-1.06	-1.2	-0.89	-1.51
D_C	149±7	69±14	24±1	166±6
K_D	12.9±1	5 ± 1.4	3.0 ± 1.0	2.9 ± 1.1
nbo/t	0.95	0.58	1.34	0.56

ΔIW is the calculated fO_2 relative to the IW buffer (see text for details).

D_c stands for the metal–silicate partitioning of carbon (mol.% of carbon in the metal / mol.% carbon in the silicate).

K_D is the distribution coefficient where $K_D = \frac{D_C}{(D_{Fe})^{n/2}}$, nbo/t is the number of non-bridging oxygen atoms over tetrahedrally coordinated cations.

The uncertainties on temperature and pressure measurements are estimated to be about 300 K and 5 GPa respectively.
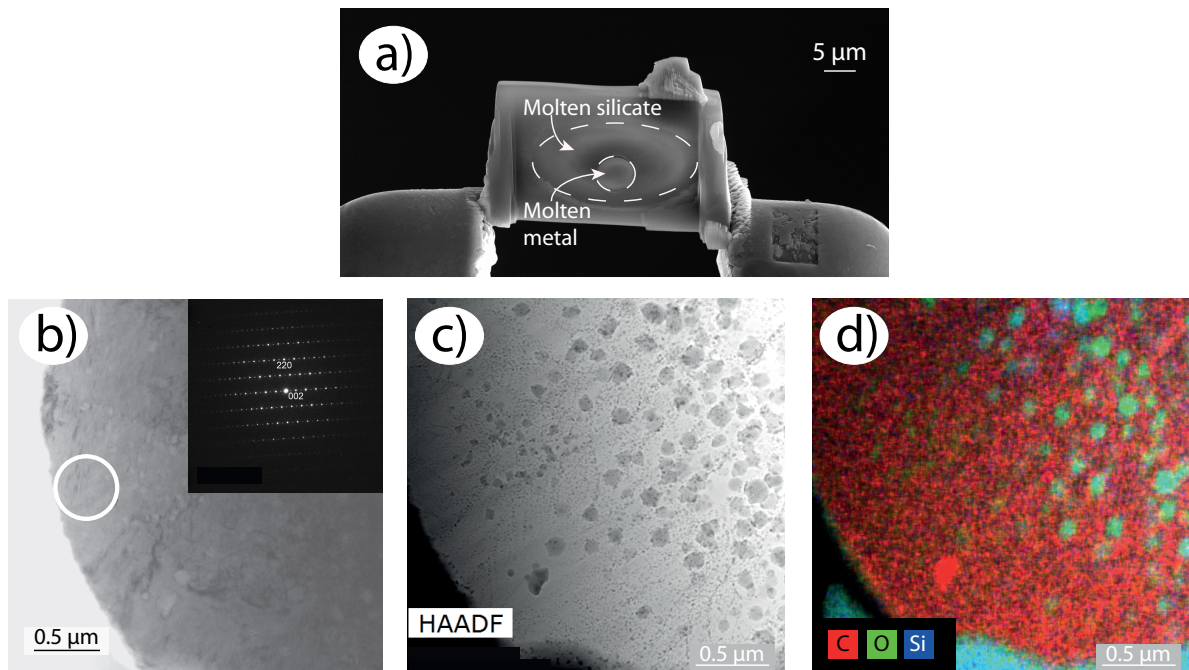
Figures

*Figure 1: **Images of run BAS C 39 synthesized at 49 GPa and 3600 K**. a) Secondary electron image where two different phases can be observed in the sample: the molten silicate and the molten metal that were equilibrated at high pressure and high temperature. b) Bright field TEM image and selected area electron diffraction pattern (Inset) of the metallic phase showing the presence of stochiometric Fe_7C_3 (also confirmed with EELS). c) High-angle annular dark field of the same sample showing exsolutions that developed during quenching along with d) Scanning TEM-EDS map of the same area which shows exsolved inclusions that are oxygen rich (green) and silicon-rich (blue). The bright red inclusion in image c) is believed to be an exsolved diamond[27].*
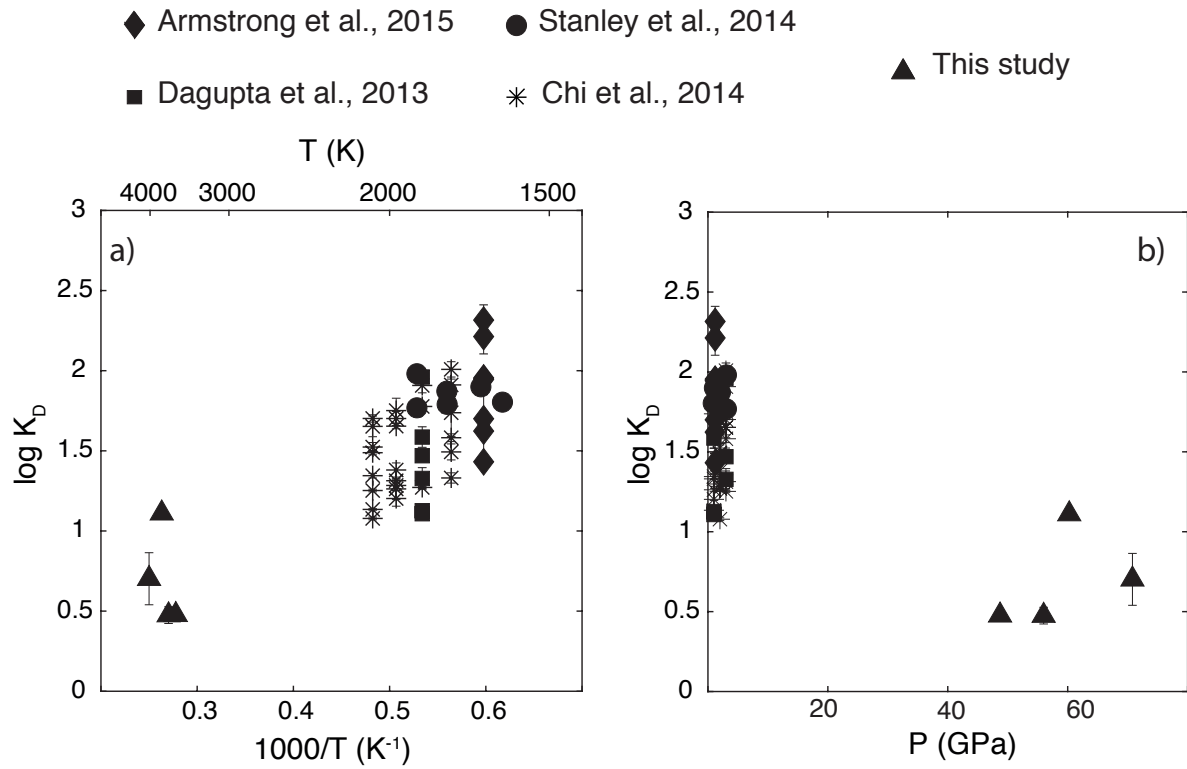
*Figure 2: **Comparison of our data with results of previous studies with respect to temperature (a) and pressure (b).** Uncertainties on temperature and pressure measurements for diamond anvil cell experiments are of 300 K and 5 GPa respectively.*
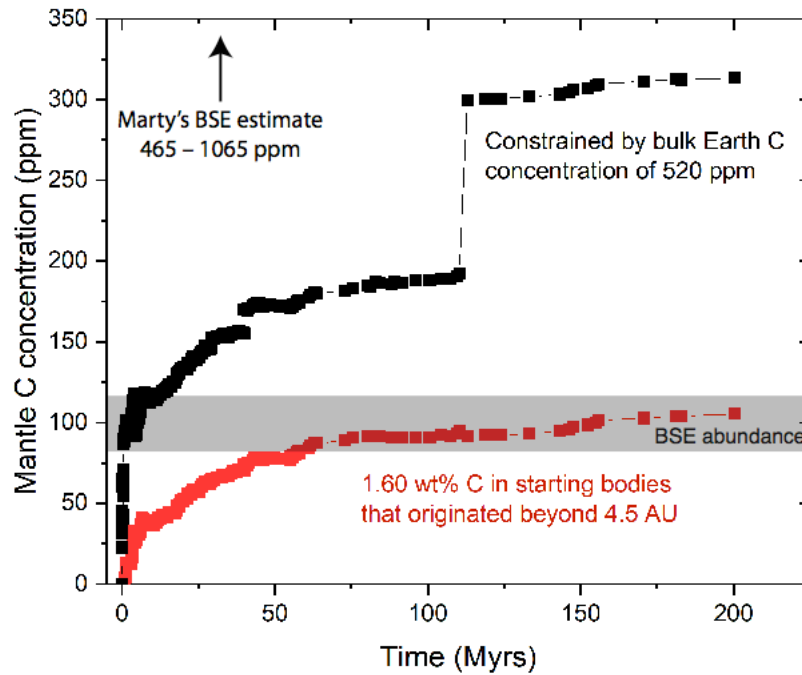
Figure 3: **Mantle C concentration during accretion as a function of time based on a combined accretion/differentiation model**[9,10]. *The red symbols show the evolution of mantle carbon concentration assuming that all starting planetesimals that originated from beyond 4.5 AU contained an average of 1.6 wt.% C; bodies originating at heliocentric distances < 4.5 AU are assumed to contain zero C. The black symbols show the evolution when the average carbon concentration in starting bodies originating from beyond 4.5 AU is 1.6 wt.% and C concentrations in bodies originating at < 4.5 AU decrease along a linear gradient to reach a value of zero at a heliocentric distance of 1.88 AU. The prominent jump at 110 Myrs is caused by the final giant impact. Estimates of the BSE concentration range from 100±20 ppm[4], as shown, to 765 ± 300 ppm[20].*

1 **Methods**

2 **a) Starting materials**

3 For the silicate starting glass, we mixed oxide and carbonate compounds in stoichiometric

4 proportions, decarbonated over night at 900°C, then added FeO. Powders were ground under

5 acetone for some time to ensure a homogeneous composition. We created pellets that were

6 subsequently fused in argon flux for several seconds at about 1400°C using a levitation furnace

7 device in Orléans, France[39]. Chemical composition of the glass was checked using EPMA

8 ("Basalt" in table S1) and we could verify that no compositional variation was detectable. The

9 glass sphere was subsequently polished down to a thickness of 20 μm and machined in IPGP,

10 France, to obtain small disks of 80 microns diameter[25].

11 The goal of this study is to understand the effect of core formation on the partitioning of carbon

12 between Earth's most important reservoirs: the silicate mantle and the metallic core. Carbon is

13 a prominent contaminant in the laboratory, with multiple sources of contamination, from the

14 use of ethanol and acetone, various type of glue or ambient contamination. It has also been

15 suggested that diamonds used as pressure transmitting tool can also diffuse carbon to the

16 samples[40]. To better understand the origin of carbon, we used ^{13}C as the source of carbon in our

17 experiments. We synthesized the metallic phase using piston-cylinder apparatus. In order to

18 assess the extent of carbon contamination during LH-DAC experiments, we only used ^{13}C. We

19 mixed 5 wt.% of ^{13}C powder (97% pure from Cambridge Isotope Laboratories, Inc.) with 95

20 wt.% of Fe. We melted this alloy at 2 GPa and 1873 K in MgO capsule for 10 minutes using a

21 ½" piston-cylinder assembly at BGI. This ^{13}C-doped carbide was then crushed to be used for

22 the metallic part of the for laser-heated diamond anvil cell experiments. The composition was

23 checked by EPMA (see table S1, "Metal") using an Fe_3C standard (see sections d) and e)).

24

25 **b) Laser-heated diamond anvil cell experiments (LH-DAC)**

26   We used diamonds with 250 μm culets and rhenium gaskets. Gaskets were pre-indented to

27   obtain a thickness of about 40 to 50 μm, and subsequently laser-drilled to have an experimental

28   chamber of about 90 μm in diameter. We then loaded two silicates discs encapsulating a flake

29   of carbide[25]. Samples were compressed to the target pressure, and then laser-heated at the

30   desired temperature using a doubled sided laser heating system at BGI. Temperature was

31   generated by two fiber continuous-wave (CW) YAG lasers (SPi©) with wavelength of 1064

32   nm and delivering 100 watts each. The laser beam was focused onto the sample using two NIR-

33   Mitutoyo objectives lenses with x20 magnification. Temperature was measured simultaneously

34   and continuously on both sides of the diamond cell using a spectro-radiometric technique[41]

35   using a 2500i spectrometer and pixis 400 CCD camera from Princeton-Instrument© from the

36   light collected through both objective lenses. The peak temperature, above the liquidus

37   temperature of the material, was maintained for few tens of seconds, before switching off the

38   electric power of the lasers to quench the experiment. The samples quenched extremely quickly

39   due to the high thermal conductivity of diamonds and the cells were subsequently decompressed

40   slowly over several hours. As observed in previous studies using LH-DAC, the silicate part

41   quenched to a glass, and the Fe-rich metal presents Si- and O-rich inclusions[24,25].

42

43   **c) Sample recovery**

44   We used the Focused Ion Beam facility (FIB, dual beam Scios FEI©) in Bayerisches Geoinstitut

45   (BGI) to recover small lamellae of 3–5 μm thickness, about 40 μm in length and 20 μm high[24,25].

46   In the samples, we observed two quenched phases that had been molten at high pressure and

47   high temperature: a silicate and metallic one (see Fig. 1-a in the main text).

48

49   **d) Fabrication of analytical standards**

50   For EPMA analysis of the carbon contents of metals, we synthesized a Fe_3C (cementite) carbide

51   standard at BGI[42], by inserting a 1 mm diameter, 10 mm long, 99.99 % purity Fe wire in a thick

52   graphite sleeve and heating it to 1423 K at 15 kbar in a piston cylinder for one week. The

53   reaction product was confirmed to have the Fe_3C cementite structure by XRD and was assumed

54   to be stoichiometric.

55   For the nanoSIMS analysis of quenched glasses, we synthesized ^{13}C-doped glass standards[43].

56   We first mixed oxides in basaltic proportions and made a glass at 1600°C in a furnace for two

57   hours. This glass was analyzed by EPMA for major elements, and by FTIR to confirm that it

58   was carbon-free ("B1" in table S1). Subsequently, we performed piston-cylinder experiments

59   to incorporate ^{13}C into the basaltic glass. The source of ^{13}C was chosen as oxalic acid enriched

60   in ^{13}C (Cambridge Isotope Laboratories, Inc.), that was loaded along with the basaltic glass in

61   a Pt capsule and pressurized to 2 GPa and heated to 1600°C for 10 minutes[43]. We created two

62   glass standards (B1145 and B1147) containing 785 ppm and 1263 ppm of carbon respectively,

63   as measured by FTIR at BGI. For the FTIR measurements, we used an extinction coefficient[44]

64   of 69500 $L.mol^{-1}.cm^{-1}$. We report the FTIR measurements along with EPMA analyses on table

65   S1 for the carbon-free (B1) and the two carbon-doped glasses.

66

67   **e) EPMA analysis**

68   Major elements from both the metallic and silicate phases were analyzed by Electron Probe

69   Microanalysis (EPMA). We calibrated using wollastonite, spinel and olivine for Ca, Al and Si,

70   Mg, Fe in the silicate respectively with current of 15 keV and 15 nA, a focused beam and a phi-

71   rho-Z correction. For the metallic phase, we used a pure Fe wire, FeSi, Fe_2O_3 and Fe_3C

72   standards to calibrate for Fe, Si, O and C respectively, at 15 keV with a 25 nA beam current,

73   again using a focused beam and phi-rho-Z correction. The counting time was 10 seconds on the

74   background, and 20 seconds on the peak for all elements, and the samples and Fe_3C standard

75   were not carbon coated.

76   Analyzing carbon using the microprobe requires special consideration[45]. In order to quantify

77   the carbon content of both the experimental metals and the metal starting material, we

78   synthesized a Fe_3C carbide primary standard (see section d)). During C analysis, we took

79   particular care in repeating the measurements on the metallic standards to quantify background

80   levels (contamination) inside the EPMA. We measured the count rate from the C kα peak on a

81   pure Fe standard continuously for ten minutes, and found no statistically-significant change in

82   peak height over that timescale[42]. We performed repeated measurements of pure iron wire to

83   check for carbon contamination, and observed a background for carbon of 0.49±0.07 wt.%

84   which is well below the amount of carbon present in the metallic phase of our samples. The

85   same was done with pure FeSi, for which we measured 0.36±0.05 wt.% of carbon in the

86   standard. As for oxygen contamination, we measured a background of 0.04±0.04 wt.% in the

87   Fe wire and 0.15±0.05 wt.% in FeSi. Those values are again well below the amount measured

88   in our samples. Standard analyses were consistent and stable over the whole duration of the

89   analytical sessions.

90   Analyses performed on the quenched silicate highlighted high concentrations of FeO (from 14

91   to 27 wt.%), as observed previously in similar experiments[24,25]. In the metallic phase, we

92   observe a range of concentrations of carbon, from 5 to 9.5 wt.%, depending on the sample.

93   Oxygen and silicon are also present in the metallic phase, from 2.8 to 7.5 wt.% oxygen and 0.3

94   to 5.6 wt.% silicon. We report on tables S2 and S3 the full analyses of our recovered runs for

95   silicate and metal respectively. Whilst some analytical totals are low, these low totals are not

96   explained by the thin samples, as a 3 μm deep lamella is thick enough to not lose electrons, nor

97   significant X-ray flux, through the base[46].

98

99 **f) nanoSIMS analysis**

100 The abundance of carbon in the silicate phase was expected to be extremely small, due to its

101 high siderophility[1]. Laser heated diamond anvil cell experiments produce very small samples,

102 with silicates phases that are only few micrometers wide. Therefore, NanoSIMS was used in

103 this study to achieve required analytical precision and spatial resolution and quantitatively

104 analyze the low carbon contents in the silicate phase.

105 NanoSIMS measurements are sensitive to matrix effects, so we took particular care in

106 synthesizing and using relevant standard glasses (see section d)). Along with those two

107 standards, we used two standards of natural rocks containing natural and known amounts of

108 carbon: a basaltic glass from the East Pacific Rise[47,48] ALV 981-R23 containing 405 ppm of

109 CO_2; and a piece of glass from D'Orbigny meteorite[49,50] containing 40 ppm of C. Composition

110 of those standards and of the natural samples are given in table S1. During the NanoSIMS

111 session, we analyzed the standards each day to check for consistency and demonstrate the

112 reproductivity of the measurements.

113 NanoSIMS analyses were performed using the CAMECA NanoSIMS 50L at the Open

114 University (Milton Keynes, UK). Prior to NanoSIMS analysis, a large area of each sample was

115 pre-sputtered using a focused primary beam of 16 KeV Cs^+ ions with probe current of 100 pA

116 to remove surface contamination. The sizes of the pre-sputtered areas vary from 5×5 to 7×7

117 μm^2. Analyses were then carried out in spot mode first by scanning a 50 pA Cs^+ beam onto the

118 inner 3×3-5×5 μm^2 areas, with secondary ions of $^{12}C^-$, $^{13}C^-$, $^{30}Si^-$, $^{24}Mg^{16}O^-$, $^{27}Al^{16}O^-$ and

119 $^{56}Fe^{16}O^-$ collected in electron multipliers simultaneously. Only the data from the inner 60% of

120 the area were collected using electron gating to avoid carbon contamination from the

121 surrounding areas. Each spot analysis consisted of 200 measurements, with a total analysis

122 time of ~2 minutes.

123   After spot analyses, selected sample areas were also measured in imaging mode. A 50 pA Cs^+

124   beam was also used in imaging mode, with five secondary ions ($^{12}C^-$, $^{13}C^-$, $^{30}Si^-$, $^{56}Fe^{13}C^-$ and

125      $^{56}Fe^{16}O^-$) monitored simultaneously. Each imaging analysis consisted of 10 frames. A frame

126   size of 256×256 pixels was used for all images with an integration time of 500 ms per pixel,

127   leading to total analysis time of 5-6 minutes for each image.

128   The mass resolving power ($m/\Delta m$) for both spot and imaging mode was set to 9000 (CAMECA

129   definition), sufficient to resolve all interferences from neighbouring mass peaks, such as ^{13}C

130   from ^{12}CH. We could extract from the region of interest (ROIs) the ratios of $^{13}C/^{30}Si$ and

131      $^{12}C/^{30}Si$. We derived a precise calibration line using those standards, which was used to infer

132   the amount of carbon (both ^{12}C and ^{13}C, see figures S1-a and S1-b) present in each of our

133   samples. During analyses, we carefully avoided metal blebs that are sometimes present in the

134   silicate phase in this style of experiments, interpreting them to be entrained rather than exsolved

135   on quench. We present in Fig. S2 NanoSIMS ion images of the metallic phase of sample BAS-

136   C-39, to highlight the level of detail that can be reached with NanoSIMS.

137   Some uncertainty of the NanoSIMS measurements may derive from the difference between the

138   composition of the samples and the one of the standards. We calculated the amount of carbon

139   in each of our samples using the C/Si ratio of the standards and the experimental runs for both

140   ^{12}C and ^{13}C. The standards we used contained between 40 and 50 wt.% of SiO_2 whereas the

141   runs contained between 35 and 40 wt.% SiO_2. To encompass the range of potential sources of

142   uncertainty, we have assigned an uncertainty of $\pm$ 15% to the nanoSIMS measurements.

143   Analysing our samples and standards with the NanoSIMS revealed that the carbon present in

144   both cases was not only ^{13}C but also ^{12}C, with a lower $^{13}C/^{12}C$ ratio in experimental silicates

145   than in the metal (values from 2.8 to 6.9 for metal versus 0.37 to 1.7 for silicate, see Fig. S1-c).

146   The presence of significant concentrations of ^{12}C was unexpected, since we carefully prepared

147   the samples using only ^{13}C, but demonstrates that carbon contamination is probably ubiquitous

148   in high-temperature DAC experiments. The silicate starting powders were heated overnight at

149   900 °C and then converted to glass using an aerodynamic levitation system at temperatures of

150   about 1400 °C. Thus, despite several hours at elevated temperatures, it is extremely hard to

151   eliminate the presence of environmental carbon. ^{12}C could originate from the diamond anvils,

152   the carbonate powders being not fully decarbonated, by sorption of carbon from the atmosphere

153   or from residues of organic carbon contamination during sample preparation.

154   The $^{13}C/^{12}C$ measured in the experimental silicates was lower than in the corresponding metals

155   (Fig. S1-c). This indicates that experiments did not reach isotopic equilibrium, and implies that

156   the most significant source of carbon contamination was the silicate starting material rather than

157   the diamond anvils. This observation is contrary to what has been proposed in previous LH-

158   DAC studies[26,40]. We also measured silicate in unmelted regions in DAC samples BAS C 39

159   and BAS C 42 at the NanoSIMS, that contained 386 and 347 ppm of carbon ($^{12}C + {}^{13}C$)

160   respectively, highlighting the presence of carbon in the starting material. We demonstrate here,

161   for the first time with support of NanoSIMS measurements, that carbon contamination in our

162   DAC experiments is not due to carbon diffusion from the diamond anvils to the samples, but is

163   from the samples themselves.

164

165   **h) TEM analysis**

166   We performed transmission electron microscope (TEM) analyses on a FEI Titan G2 80-200

167   S/TEM equipped with X-ray energy dispersive spectrometer (EDS) and electron energy-loss

168   spectrometer (EELS) in Bayerisches Geoinstitut in order to observe and further analyze the

169   experimental metals. To do so, we further thinned down one of our samples to a thickness of

170   60-80 nm using FIB. The FIB lamella was plasma cleaned prior to TEM analysis in order to

171   remove surface contamination. We determined Fe/C ratios in our sample and also perform EDS

172   mapping in the metallic phase. The quantification of the EELS analyses followed the procedure

173 previously described[40,51], using experimentally-determined ratios of partial cross sections of C

174 K and O K edges against the Fe L edge versus sample thickness, which were calibrated with

175 synthetic $Fe_{0.94}O$ and Fe_3C samples. Note that due to the inhomogeneity of the metallic phase

176 of the sample (see Fig. 1-a,-b,-c), EELS technic cannot provide a measurement of the bulk

177 carbon contents of this phase.

178

179 **Bibliography**

180 39.   Auzende, A.-L. *et al.* Synthesis of amorphous MgO-rich peridotitic starting material
181   for laser-heated diamond anvil cell experiments–application to iron partitioning in the
182   mantle. *High Press. Res.* **31**, 199–213 (2011).

183 40.   Fischer, R. A. *et al.* High pressure metal-silicate partitioning of Ni, Co, V, Cr, Si, and
184   O. *Geochim. Cosmochim. Acta* **167**, 177–194 (2015).

185 41.   Benedetti, L. R. & Loubeyre, P. Temperature gradients, wavelength-dependent
186   emissivity, and accuracy of high and very-high temperatures measured in the laser-
187   heated diamond cell. *High Press. Res.* **24**, 423–445 (2004).

188 42.   Dasgupta, R. & Walker, D. Carbon solubility in core melts in a shallow magma ocean
189   environment and distribution of carbon between the Earth's core and the mantle.
190   *Geochim. Cosmochim. Acta* (2008). doi:10.1016/j.gca.2008.06.023

191 43.   Yoshioka, T., McCammon, C., Shcheka, S. & Keppler, H. Letter. the speciation of
192   carbon monoxide in silicate melts and glasses. *Am. Mineral.* **100**, 1641–1644 (2015).

193 44.   Fine, G. & Stolper, E. Dissolved carbon dioxide in basaltic glasses: concentrations and
194   speciation. *Earth Planet. Sci. Lett.* (1986). doi:10.1016/0012-821X(86)90078-6

195 45.   Dasgupta, R. & Walker, D. Carbon solubility in core melts in a shallow magma ocean
196   environment and distribution of carbon between the Earth's core and the mantle.
197   *Geochim. Cosmochim. Acta* **72**, 4627–4641 (2008).

198 46.   Jennings, E. S., Wade, J., Laurenz, V. & Petitgirard, S. Diamond anvil cell partitioning
199   experiments for accretion and core formation: Testing the limitations of electron
200   microprobe analysis. *Microsc. Microanal.* **25**, 1–10 (2019).

201 47.   Macpherson, C. G., Hilton, D. R., Newman, S. & Mattey, D. P. CO2,13C/12C and
202   H2O variability in natural basaltic glasses: A study comparing stepped heating and
203   FTIR spectroscopic techniques. *Geochim. Cosmochim. Acta* (1999).

204   doi:10.1016/S0016-7037(99)00124-6

205   48.   Hekinian, R. & Walker, D. Diversity and spatial zonation of volcanic rocks from the

206   East Pacific Rise near 21° N. *Contrib. to Mineral. Petrol.* **96**, 265–280 (1987).

207   49.   Abernethy, F. A. J. *et al.* Stable isotope analysis of carbon and nitrogen in angrites.

208   *Meteorit. Planet. Sci.* **48**, 1590–1606 (2013).

209   50.   Varela, M. E. *et al.* Glasses in the D'Orbigny angrite. *Geochim. Cosmochim. Acta* **67**,

210   5027–5046 (2003).

211   51.   Miyajima, N. *et al.* Combining FIB milling and conventional Argon ion milling

212   techniques to prepare high-quality site-specific TEM samples for quantitative EELS

213   analysis of oxygen in molten iron. *J. Microsc.* (2009). doi:10.1111/j.1365-

214   2818.2009.03341.x

215

Extended Data Tables and Figures

217

218 *Table S1: Composition of the synthetic basaltic starting silicate used for the LH-DAC*

219 *experiments ("Basalt"), the standards for the NanoSIMS synthesized with piston-cylinder at 2*

220 *GPa and 1600℃ ("B1145" and "B1147"), the carbon-free starting material for piston-*

221 *cylinder experiments ("B1") and the starting metal used in LH-DAC experiments. We also*

222 *report the composition of the two natural samples that were used at the NanoSIMS as*

223 *standards. b.d. stands for below detection limit.*

Samples	Basalt	B1145	B1147	B1	D'Orbigny glass[a]	ALV 981-R23[c]		Metal
wt.%	*N=10*	*N=7*	*N=7*	*N=7*	-	-		*N=14*
SiO_2	52.18 (0.15)	48.05 (0.18)	50.89 (0.27)	53.56 (0.13)	41.7	49.63	C	5.67 (1)
Na_2O	1.90 (0.03)	1.80 (0.06)	1.86 (0.06)	2.03 (0.03)	-	2.91	Fe	91.61 (1.31)
CaO	10.92 (0.07)	9.47 (0.10)	10.03 (0.08)	10.70 (0.05)	23.3	11.61		
FeO	11.35 (0.04)	13.65 (0.20)	10.71 (0.06)	10.04 (0.06)	11.0	8.16		
Al_2O_3	14.66 (0.07)	16.37 (0.11)	15.22 (0.10)	15.48 (0.05)	19.6	16.60		
MgO	7.45 (0.07)	7.22 (0.08)	7.57 (0.10)	7.73 (0.06)	1.87	8.36		
C (ppm)	-	785 (8)*	1263 (13)*	b.d.*	40	111		
Total	98.46 (0.20)	96.66 (0.19)	96.41 (0.33)	99.55 (0.15)	99.3[b]	98.96[d]		97.28 (0.76)

224 *Measured using FTIR (see text for details)
225 [a] Composition from ref.[50]
226 [b] Total includes also 2 wt.% of TiO_2, Cr_2O_3, MnO
227 [c] Composition from refs.[47,48]
228 [d] Total includes TiO_2, MnO, K_2O and P_2O_5

229
230 *Table S2: Compositions of quenched silicate liquid. Major elements were analysed using*

231 *EPMA and carbon was analysed using NanoSIMS. See text for details.*

Run #	BAS C 50	BAS C 60	BAS C 39	BAS C 42
wt.%	*N=4*	*N=5*	*N=8*	*N=6*
SiO_2	35.84 (0.38)	39.97 (1.98)	34.09 (0.83)	39.66 (0.99)
MgO	8.85 (0.20)	8.60 (0.28)	9.53 (0.51)	9.02 (0.26)
Al_2O_3	19.46 (0.12)	25.93 (0.50)	16.34 (1.36)	24.48 (0.64)
CaO	4.02 (0.16)	4.89 (0.12)	5.67 (0.20)	5.68 (0.31)
Na_2O	2.13 (0.07)	2.22 (0.10)	2.32 (0.15)	2.53 (0.11)
FeO	23.82 (1.40)	18.60 (0.60)	27.35 (2.55)	13.71 (1.72)
C (ppm)*	312 (47)	545 (82)	2805 (420)	272 (41)
Total	94.12 (1.85)	100.2 (1.96)	95.30 (2.34)	95.07 (1.55)

232 *15% uncertainties estimated on NanoSIMS measurements (see text for more details).

233

234 *Table S3: Composition of the metal phase of our recovered runs analysed using EPMA. See*
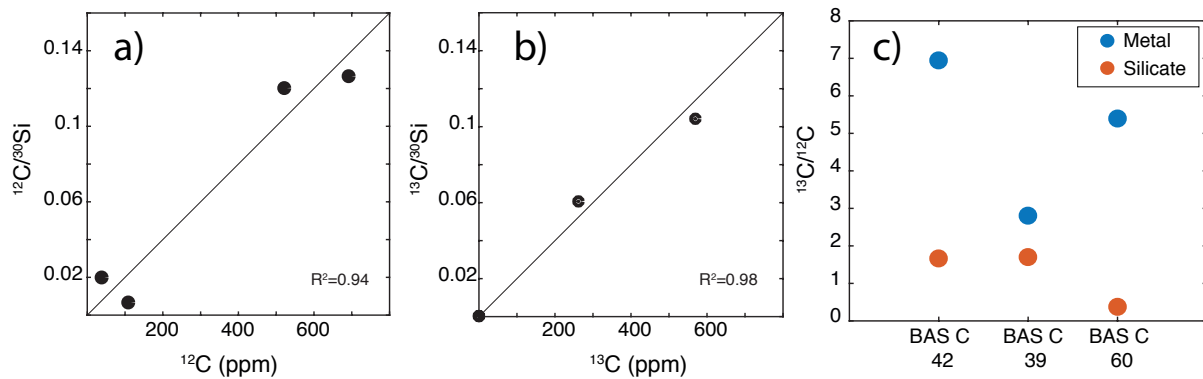
235 *text for details.*

Run #	BAS C 50	BAS C 60	BAS C 39	BAS C 42
EPMA (wt.%)	*N=3*	*N=3*	*N=4*	*N=2*
Fe	*81.68 (1.25)*	*79.56 (0.9)*	*85.96 (0.58)*	*78.01 (0.78)*
Si	*0.46 (0.16)*	*5.56 (0.16)*	*0.33 (0.11)*	*2.65 (0.40)*
O	*3.79 (0.89)*	*7.56 (0.37)*	*2.85 (0.48)*	*3.42 (0.10)*
C	*5.90 (0.18)*	*4.99 (0.28)*	*9.44 (0.24)*	*5.35 (0.20)*
Total	*91.83 (0.41)*	*97.66 (0.38)*	*98.57 (0.29)*	*89.43 (0.48)*

236

237
238

239

240 *Figure S1:**Results from NanoSIMS measurements.** a) and b) calibration lines obtained for*

241 *^{12}C and ^{13}C respectively using our standards and two natural samples (d'Orbigny and ALV*

242 *981-R23) and both FTIR and NanoSIMS measurements. Note that for ^{13}C measurements, the*

243 *two natural samples plot at 0. c) Illustration of the isotopic disequilibrium between the*

244 *metallic and the silicate phase for three of our recovered runs which illustrates the presence*

245 *of ^{12}C in our reacted samples, despite the use of pure ^{13}C in the starting material.*
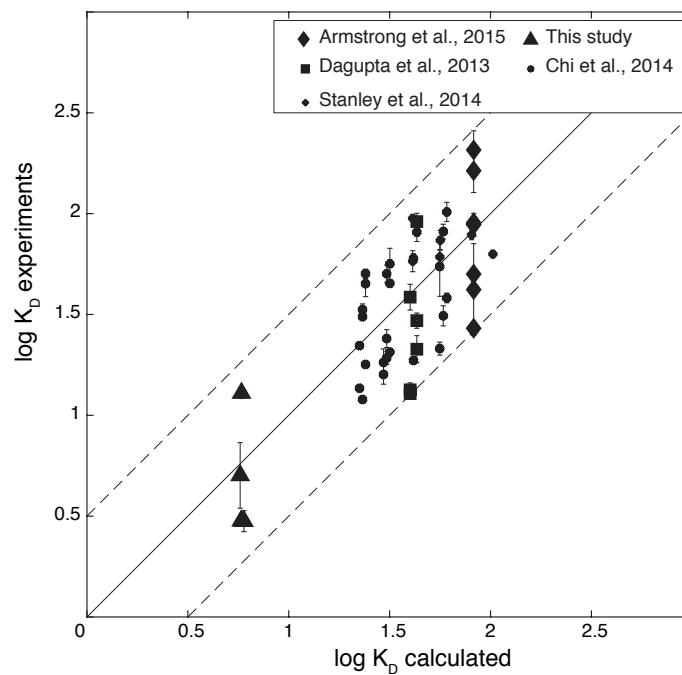
246

247
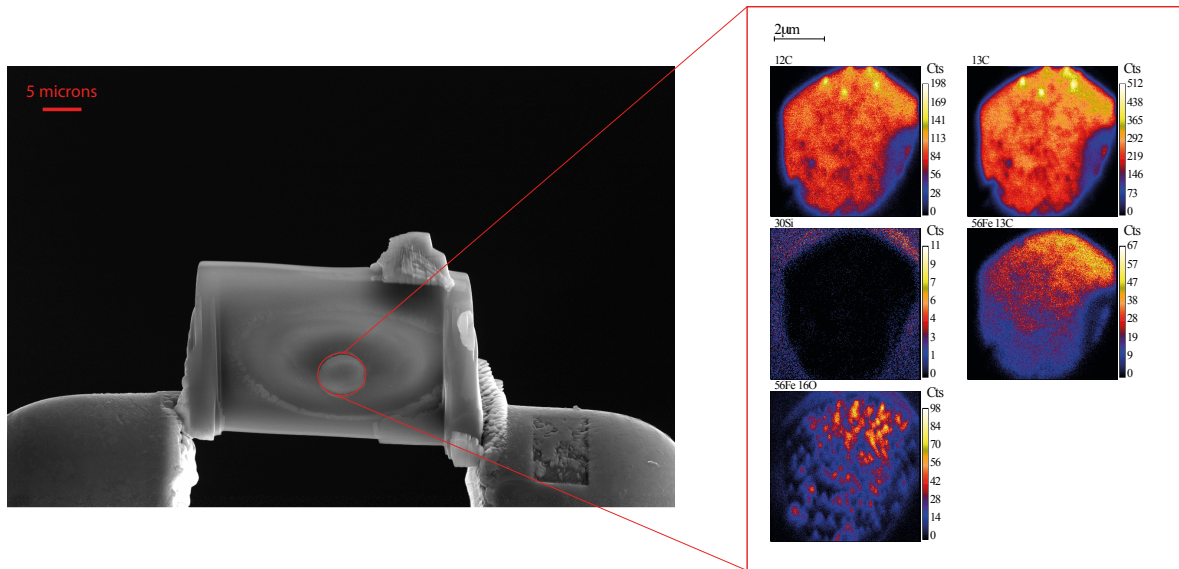
Figure S2: Secondary electron image of sample BAS-C-39 along with NanoSIMS mapping of

the metallic phase.

250
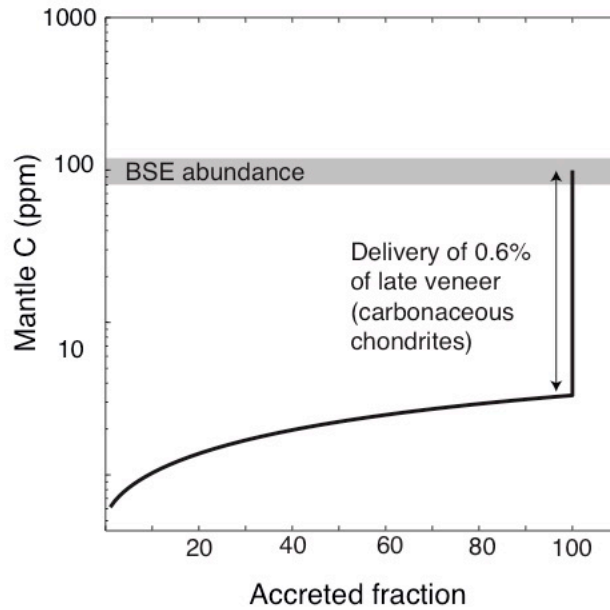

251

*Figure S3: **Validation of our partitioning model**. Comparison of the K_D values (see eq. 3 in*

the main text) calculated from the experiments and from our model (eq. 4 in the main text).

254

255

*Figure S4: **Continuous core formation model**. Evolution of the concentration of carbon in*

the mantle during Earth's core–mantle differentiation and the late accretion stage based on a

continuous core formation model. The estimated BSE concentration of 80–120 ppm is shown

in both cases[4].

271   Advanced Grant "ACCRETE" (contract 290568). The Scios Focus Ion Beam at BGI was

272   financed by a DFG grant No. INST 91/315-1 FUGG.

273

274   **Authors contributions**

275   I.B. conceived the project, performed experiments, analyzed data and derived the

276   thermodynamic model. E.S.J. analyzed data. I.A.F., X.Z. performed NanoSIMS measurements.

277   S.P. performed laser heating experiments and helped with FIB. N.M. performed TEM

278   measurements. D.C.R. and S.A.J. built the accretion model. I.B., E.S.J. and D.C.R wrote the

279   manuscript.

280

281   **Additional information**

282   **Supplementary Information** is available for this paper. Correspondence and requests for

283   materials should be addressed to Ingrid Blanchard (ingrid.blanchard@uni-bayreuth.de).

284

285   **Supplementary Information**

286   Using our high pressure and high temperature experiments along with the ones of the literature,

287   we built a new parameterization for the metal–silicate partitioning of carbon (Eq. 4 in the main

288   text). We compare in Fig. S3 the agreement between the experimental K_D and the one predicted

289   by our regression. Then, we utilized two styles of modelling in this study. The first one is the

290   one presented in the main text, and the second one is a more simple continuous core formation

291   model that has been applied in many geochemical studies[1–3]. Here, Earth is assumed to accrete

292   material in small (1%) increments and each batch of accreted metal is assumed to equilibrate

293   chemically with the entire mantle. The equilibration pressure is assumed to correspond to

294   conditions the base of the magma ocean and increases as the planet grows. The temperature at

295   the base of the magma ocean, which is constrained by the peridotite solidus–liquidus, also

296   increases as the Earth grows. For simplicity, we set the fO$_2$ during accretion at IW-2.3 as given

297   by the current mantle/core FeO/Fe ratio[4].

298   The concentration of carbon in the mantle today is estimated to lie between 80 and 120 ppm

299   (Dasgupta and Hirschman 2010; Hirschman 2016). On the other hand, the bulk Earth carbon

300   content has been proposed to lie between 520 ppm[5] and 750 ppm[6]. Here, we assume that each

301   stepwise-accretion step delivers material with a bulk C content that matches the bulk Earth

302   value[5]. Using the higher value of 750 ppm[6] would not significantly change the results. The

303   partition coefficient of carbon is calculated after each equilibration step following eq. 4, and

304   the resulting amount of carbon present in both mantle and core is derived from this calculation.

305   Hence, carbon is present throughout accretion.

306   The Earth is believed to have been bombarded by bodies comprised of chondritic material after

307   core formation ceased (the so-called late accretion stage which resulted in addition of the "late

308   veneer") in order to explain the concentrations of highly siderophile elements present in the

309   mantle[7–9]. The amount of material that was delivered to Earth during late accretion was about

310   0.6% of Earth's mass[10], and was not incorporated into the core, but rather remained in the

311   mantle. Chondrites are carbon-rich, with up to 3.2 wt.% of carbon reported in CI chondrites[11],

312   so their delivery to Earth brought a substantial amount of carbon. We incorporated the effect of

313   such late accretion in our model by assuming that the carbon content of the late veneer matches

314   the mean carbonaceous chondrite (CI, CM, CO and CV) value of 1.6 wt.%.

315   Results of the continuous core formation model are presented in Fig. S4. The combined effects

316   of core formation and later addition of late veneer are needed in order to reproduce the carbon

317   content of the BSE. Core–mantle differentiation effectively strips the mantle of all carbon and

318   the addition of C during late accretion is required to achieve the mantle carbon concentration.

319   According to this model, the resulting concentration of carbon in the core after the combined

320   effect of differentiation and late veneer is 0.16 wt.%. This result is consistent with previous

321   suggestions, based on first principles molecular dynamics[12] and experiments[13], that carbon is

322   not a dominant element in Earth's core. As discussed in the main text, this simple scenario is

323   not coherent with astrophysical accretion scenarios. This model assumes that the bulk Earth C-

324   content is known *a priori*, and the assumption that all accreted metal equilibrate with all the

325   mantle is also unrealistic.

326

327   **Bibliography**

328   1.   Wade, J. & Wood, B. J. Core formation and the oxidation state of the Earth. *Earth*

329   *Planet. Sci. Lett.* **236**, 78–95 (2005).

330   2.   Wood, B. J., Walter, M. J. & Wade, J. Accretion of the Earth and segregation of its

331   core. *Nature* **441**, 825–833 (2006).

332   3.   Righter, K. *et al.* Volatile element signatures in the mantles of Earth, Moon, and Mars:

333   Core formation fingerprints from Bi, Cd, In, and Sn. *Meteorit. Planet. Sci.* **53**, 284–305

334   (2018).

335   4.   Corgne, A., Siebert, J. & Badro, J. Oxygen as a light element: A solution to single-

336   stage core formation. *Earth Planet. Sci. Lett.* **288**, 108–114 (2009).

337   5.   Marty, B. The origins and concentrations of water, carbon, nitrogen and noble gases on

338   Earth. *Earth Planet. Sci. Lett.* (2012). doi:10.1016/j.epsl.2011.10.040

339   6.   McDonough, W. F. & Sun, S. The composition of the Earth. *Chem. Geol.* **120**, 223–

340   253 (1995).

341   7.   Chou, C., Shaw, D. M., Crocker, J. H., Ridge, R. & Schilling, S. Siderophile trace

342   elements in the Earth' oceanic crust and upper mantle. *J. Geophys. Res.* (1983).

343   8.   Turekian, K. K. & Clark, S. P. Inhomogeneous accumulation of the earth from the

344   primitive solar nebula. *Earth Planet. Sci. Lett.* **6**, 346–348 (1969).

345   9.   Kimura, K., Lewis, R. S. & Anders, E. Distribution of gold and rhenium between

346   nickel-iron and silicate melts: implications for the abundance of siderophile elements

347   on the Earth and Moon. *Geochim. Cosmochim. Acta* **38**, 683–701 (1974).

348   10.   Walker, R. J. Highly siderophile elements in the Earth , Moon and Mars : Update and

349   implications for planetary accretion and differentiation. *Chemie der Erde-*

350   *Geochemistry* **69**, 101–125 (2009).

351   11.   Wasson, J. T. & Kallemeyn, G. W. Compositions of chondrites. *Philos. Trans. R. Soc.*

352   *London A Math. Phys. Eng. Sci.* **325**, 535–544 (1988).

353   12.   Zhang, Y. & Yin, Q.-Z. Carbon and other light element contents in the Earth's core

354   based on first-principles molecular dynamics. *Proc. Natl. Acad. Sci.* **109**, 19579–19583

355   (2012).

356   13.   Mashino, I., Miozzi, F., Hirose, K., Morard, G. & Sinmyo, R. Melting experiments on

357   the Fe–C binary system up to 255 GPa: Constraints on the carbon content in the Earth's

358   core. *Earth Planet. Sci. Lett.* **515**, 135–144 (2019).

359